ACS APPLIED ENERGY MATERIALS

www.acsaem.org Article

A Generalized Synthesis Strategy for Binderless, Free-Standing Anode for Lithium/Sodium Ion Battery Comprised of Metal Selenides@Carbon Nanofibers

Zizhou He, Hui Guo, Jed D. LaCoste, Don Werder, Derek J. Durocher, Ryan A. Cook, Phat Truong, Hongmei Luo, Xiao-Dong Zhou,* and Ling Fei*

Cite This: *ACS Appl. Energy Mater.* 2022, 5, 842−851 Read Online

ACCESS | Metrics & More | Article Recommendations | Supporting Information

Downloaded via CORNELL UNIV on February 15, 2022 at 17:22:18 (UTC).
See https://pubs.acs.org/sharingguidelines for options on how to legitimately share published articles.

ABSTRACT: The craving for lighter, smaller, and longer-lasting portable devices has driven researchers to explore next-generation materials for both lithium-ion batteries (LIBs) and sodium-ion batteries (SIBs). Metal selenides are a notable material family that exhibits desirable conductivity, stability, and cost-effectiveness. Moreover, they can provide higher theoretical capacities than that of a commercial graphite anode. Herein, we report a generalized synthesis strategy to achieve free-standing metal selenides and carbon nanofibers composites (MSe@CNFs) as anodes for LIBs and SIBs by using facile electrospinning. The composites have active nanoparticles embedded in each carbon nanofiber, and the carbon nanofibers intertwine with each other to form a 3D nanofiber network. The structure−property−performance relationship of metal selenides (MSe, M = Sn, Fe, Ni, Cu) embedded in CNFs were thoroughly investigated in the LIBs system. The one-step prepared free-standing anodes show a high specific capacity as well as good rate capability and cycle stability. The good performance is ascribed to the high electron conductivity originating from the N-doped carbon nanofiber network, fast electrolyte penetration through interfiber voids, and accommodation of volume change enabled by the carbon encapsulation of nanoparticles. Additionally, the absence of the binder, additive carbon, and current collector not only reduces the weight of the anode but also eliminates the uncontrollable structure formation from the slurry coating method. Postmortem analysis further confirms the robust structural stability of these rationally designed composites. When the application is extended to SIBs, the composites also demonstrate great potential. In short, free-standing MSe@CNFs composites show great promise for the next generation of flexible and lightweight batteries that are crucial for various emerging applications.

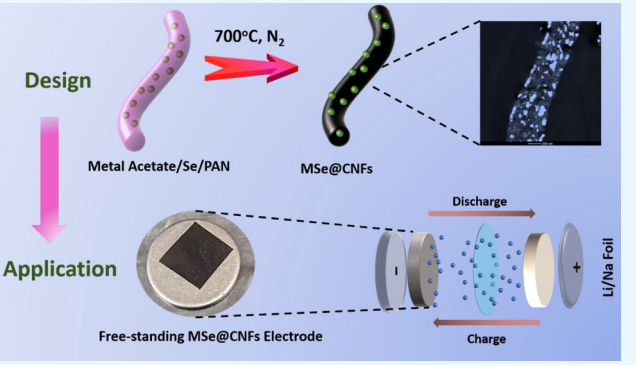

KEYWORDS: *metal selenides, carbon nanofibers, electrospinning, free-standing anode, batteries*

1. INTRODUCTION

During the past decade or so, the ever-growing electric vehicle and portable electronic sectors have significantly driven the development of lightweight, high-energy-density, and long-lifespan batteries.[1−3] The widely used lithium-ion batteries (LIBs) are limited by the capacity of electrode materials as well as the scarcity of resources (i.e., lithium and cobalt).[4−6] Particularly, graphite is the current commercial anode material for LIBs, but exhibits a low theoretical capacity of 372 mA h g^{-1} for LIBs and 35 mA h g^{-1} for sodium-ion batteries (SIBs).[7] To address these challenges, much has been done to develop new anode materials for LIBs and explore batteries beyond lithium. Low-cost and earth-abundant sodium has physical and chemical properties akin to lithium. Hence, the designed materials will also be evaluated for their potential in SIBs.

Compared to graphite, metal oxides, sulfides, and selenides have gained increasing attention because of their higher theoretical capacity and flexible chemistry.[8−13] Among them, metal oxides generally suffer large volume expansion and poor conductivity.[14] Metal sulfides have poor life cycles because of the shuttling effects caused by the generation of polysulfides.[15] As for metal selenides, they present better electronic conductivity compared to metal oxides and sulfides because of smaller band gaps.[16,17] The 3d orbital of Se could participate in bonding with metal atoms because of its energy level being close to the 3s and 3p orbitals. Such electron structure leads to more metallicity in transition-metal selenides compared to that

Received: October 18, 2021
Accepted: December 3, 2021
Published: December 16, 2021

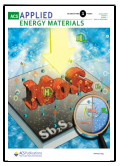

ACS Publications © 2021 American Chemical Society

of metal sulfides, which is beneficial for electron transport and reaction occurrence.[18] These advantages indicate metal selenides could potentially manifest good electrochemical performance. Lots of efforts have been devoted to studying the electrochemical properties and performance of metal selenides as battery anode materials.[19] Carbon matrixes are often incorporated to metal selenides, allowing for accommodation of the volume change, and further enhancing the electrical conductivity. For instance, Huang et al. incorporated $SnSe_2$ quantum dots with reduced graphene oxide as an anode for LIBs, which delivered an excellent rate capacity of 778.5 and 324.5 mA h g^{-1} at 50 and 5000 mA g^{-1}, respectively.[20] Wang's group reported a yolk−shell FeSe@C nanobox with 871.6 mA h g^{-1} up to 250 cycles in LIBs at 1 A g^{-1}.[21] Gao et al. synthesized NiSe of varied morphologies with N-doped carbon encapsulation for LIBs, which demonstrated good electrochemical performance (279 mA h g^{-1} at 2 A g^{-1} for up to 150 cycles).[22] Metal selenides were also found to be promising for SIBs. Microflower-like FeSe@carbon nanosheet composites showed a specific capacity of 214.6 mA h g^{-1} with a high capacity retention of 99.9% after 140 cycles at 1 A g^{-1}.[23] Dong et al. proposed a $FeSe_2$@C microspheres electrode with a capacity of 428 mA h g^{-1} after 1000 cycles.[24] A 3D pollen-scaffolded NiSe@MOF-derived carbon shell reported by Su et al. for Na^+ storage achieved a capacity of 598.2 mA h g^{-1} after 100 cycles at 200 mA g^{-1}.[25] Overall, great progress has been achieved in metal selenides as battery anode materials.[26,27] However, most reported work focuses on one specific metal selenide and requires tedious synthesis methods. The obtained materials are often in a powder form, still requiring slurry coating steps for electrode preparation. The slurry coating method has an inactive binder and conductive carbon added to active materials. These additives as well as current collectors do not contribute to the capacity, instead only add extra weight and cost to the electrode.[28] Moreover, the slurry-based electrodes tend to form undesired interfaces, uncontrollable microstructure, and limited surface area.[29,30] Therefore, it is of great interest to develop free-standing anode materials that bypass the slurry coating procedure and significantly reduce the weight of batteries with no binder, extra conductive materials, and current collectors involved.

Herein, we report a general facile and scalable electrospinning approach with a subsequent heat treatment to fabricate a series of metal selenides and carbon composites as free-standing anode materials without binder. Specifically, metal selenides (MSe, M = Sn, Fe, Ni, and Cu) embedded in a carbon nanofiber network (MSe@CNFs) were prepared and directly used as anodes in LIBs and SIBs. The prepared materials have the following advantages: (i) instead of the multistep preparation, electrospinning with subsequent heat treatment can directly incorporate active metal selenides into nitrogen-doped carbon nanofibers matrixes as free-standing electrodes, eliminating additives and bypassing the slurry coating steps;[31,32] (ii) intertwined 3D carbon nanofibers networks act like highways for electron transfer. The numerous interfiber voids provide an easy access of the electrolyte to active sites as well as accommodate volume expansion during cycling;[33] (iii) not only does the structure of metal selenide sites embedded in the fiber help avoid agglomeration of active materials, but also the nanosized feature shortens the pathway of Li- or Na-ion diffusion and thus promotes ion-transfer rate and reaction kinetics.[34−36] With these advantages, the designed MSe@CNFs demonstrate highly stable cyclability and robust rate performance in LIBs as well as great potential for SIBs. This facile synthesis approach provides a promising way to fabricate lightweight and high-performance metal selenides materials for battery applications.

2. EXPERIMENTAL SECTION

Synthesis of MSe@CNFs. *N*,*N*-Dimethylformamide (DMF, ACS grade, VWR), nickel(II) acetate tetrahydrate ($Ni(OCOCH_3)_2{\cdot}4H_2O$, 98%, Sigma-Aldrich), tin(II) acetate ($Sn(OCOCH_3)_2$, Sigma-Aldrich), iron(II) acetate ($Fe(OCOCH_3)_2$, 95%, Sigma-Aldrich), Copper(II) acetate hydrate ($Cu(OCOCH_3)_2{\cdot}xH_2O$, 98%, Sigma-Aldrich), selenium (Se, ≥99.5%, powder 100 mesh, sublimated, Alfa Aesar), polyacrylonitrile (PAN, average M_w 150 000, Sigma-Aldrich) were used directly without further purification.

In a typical procedure, 0.5 g of PAN was dissolved in a 5 mL DMF solvent at 80 °C overnight to obtain a homogeneous PAN solution. Then 2.3 mmol of metal acetate was added to the above solution and stirred for 1 h, followed by the addition of 0.5 g of selenium powder into the solution. The precursor solution was well dispersed through ultrasonication and vigorous stirring.

The degassed precursor solution was then loaded into a syringe and fitted in a syringe pump (Harvard apparatus, USA). Electrospinning was carried out to make the fresh metal acetate/Se/PAN fiber mats, whereas DMF solvent evaporated simultaneously during this process. The electrospinning parameters, including a needle gauge, voltage, infusion rate, and the distance between the needle and aluminum foil collectors, were fixed at 20-gauge, 17.5 kV, 12 μL min^{-1}, and 15 cm, respectively. The obtained fiber mats were carefully peeled off from the grounded metal collector and transferred into a tube furnace for heat treatment. The fiber mat was annealed at 700 °C for 1 h under a nitrogen atmosphere with a ramp rate of 5 °C min^{-1} to yield MSe@CNFs.

Characterizations. Morphological analysis of MSe@CNFs was performed by using Tescan Mira3 field-emission scanning electron microscopy and FEI F20 field-emission scanning transmission electron microscopy operating at 200 kV. The crystal structural characterizations were determined by recording diffraction patterns of the samples using an X-ray diffractometer (Rigaku D/Max2500) with a Cu Kα X-ray source at a scanning speed of 3° min^{-1} at a 2θ range of 10−80°. The carbon content was determined by thermogravimetric analysis (TGA). TGA samples were analyzed in an air atmosphere from room temperature to 800 °C with a ramp rate of 10 °C min^{-1}. X-ray photoelectron spectroscopy (XPS) measurements were performed with an Al Kα X-ray source.

Battery Preparation and Electrochemical Measurement. The obtained free-standing MSe@CNFs were cut into the desired shape and weight and directly used as anode electrodes for LIBs and SIBs. For LIBs, the electrochemical performance of the electrodes was investigated in CR2032 coin cells using lithium metal foil as the counter and reference electrodes in half cells and commercial-grade $LiFePO_4$ as the cathode (MTI Corporation, USA) for the full cell. Celgard 2400 was used as the separator. $LiPF_6$ (1 M) in a mixture of ethylene carbonate/dimethyl carbonate/diethyl carbonate (EC/DMC/DEC, 1:1:1 in volume) solution was used as the electrolyte. For SIBs, sodium metal foil was used as counter and reference electrodes and glass fiber paper as separator. 1 M $NaPF_6$ in a mixture of ethylene carbonate/diethyl carbonate (EC/DEC 1:1 in volume) solution was the electrolyte. All the coin cells were assembled in an argon-filled glovebox with an oxygen and water content level lower than 1 ppm. Cyclic voltammetry was measured with a STAT III electrochemical workstation (Princeton Applied Research, USA) at a scan rate of 0.2 mV min^{-1} in the voltage window of 0.05−3 V versus lithium (vs Li^+/Li) for LIBs and in the voltage window of 0.005−2.5 V versus sodium (vs Na^+/Na) for SIBs. The galvanostatic charge/discharge measurements were performed by using a Landt battery testing system in the voltage window of 0.05−3 V (vs Li^+/Li) and 0.005−2.5 V (vs Na^+/Na) for LIBs and SIBs, respectively.

https://doi.org/10.1021/acsaem.1c03277
ACS Appl. Energy Mater. 2022, 5, 842−851

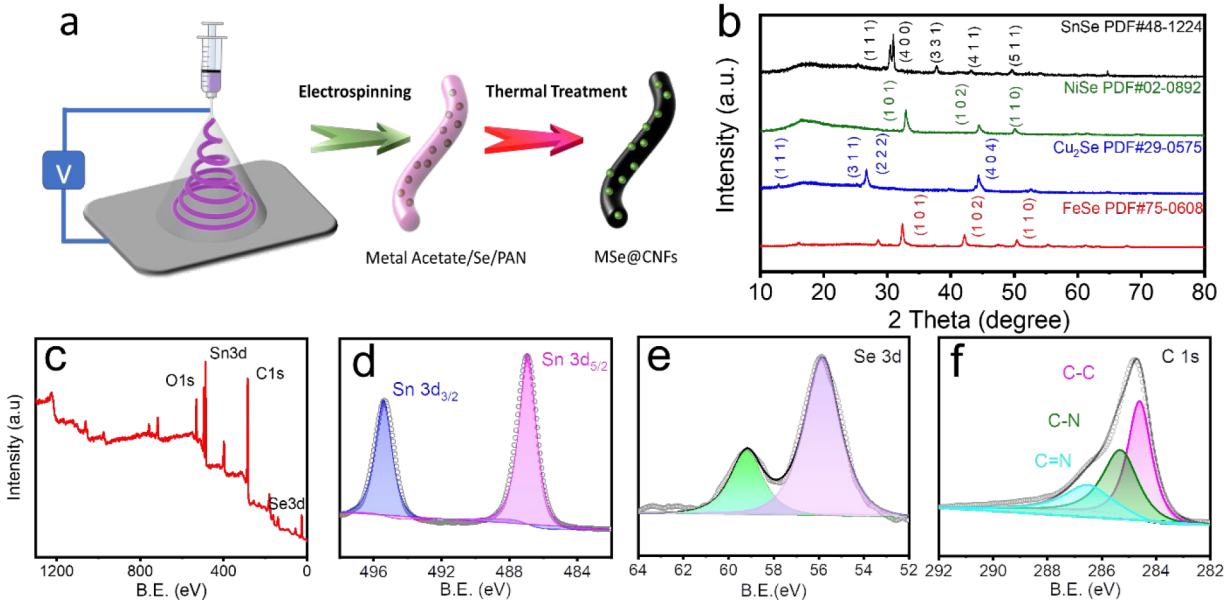

Figure 1. (a) Schematic illustration of the synthetic procedure of MSe@CNFs; (b) XRD pattern of MSe@CNFs; (c) full survey of SnSe@CNFs; (d–f) high-resolution XPS spectra of Sn 3d, Se 3d, and C 1s of SnSe@CNFs.

3. RESULTS AND DISCUSSION

The synthesis procedure is schematically illustrated in Figure 1a. In general, PAN/DMF polymer solution is prepared first, and then a certain amount of metal acetates are dissolved in the solution. Subsequently, selenium powder is uniformly dispersed into the solution via stirring and ultrasonication. Fresh MSe@CNFs nanofiber mat is prepared via electrospinning of the precursor solution. The as-spun fiber mats are then annealed in nitrogen to obtain free-standing MSe@CNFs (digital images in Figure S1, Supporting Information). During the heat treatment, selenium and metal acetates react with each other to form MSe nanoparticles. Meanwhile, PAN polymer backbones are converted to carbon nanofibers that intertwine with each other and form a unique 3D network structure.

The obtained samples are then subjected to XRD analysis for the study of their phase and crystallinity. The XRD patterns of the samples are shown in Figure 1b with all the major peaks labeled. As can be seen, the characteristic peaks of each sample can be well indexed, corresponding to SnSe (JCPDS No. 48-1224), NiSe (JCPDS No. 02-0892), Cu_2Se (JCPDS No. 29-0575), and FeSe (JCPDS No. 75-0608), respectively. No selenium peak is observed, indicating the excess selenium is sublimated during the annealing process. Through TGA analysis (Figure S2), the weight percentages of SnSe, FeSe, Cu_2Se, and NiSe in the MSe@CNFs composites are determined to be 44.38%, 49.84%, 32.31%, and 49.41%, respectively.

XPS is conducted to further understand the surface composition and chemical states of the samples. The full survey of SnSe@CNFs is shown in Figure 1c where Sn 3d, C 1s, Se 3d, and O 1s can be identified. The presence of O 1s may be due to unavoidable surface oxygen absorption when exposed to air and partial oxidation of surface MSe. In Figure 1d, the observed peaks at ~495.4 and ~486.9 eV are identified as the Sn $3d_{3/2}$ and Sn $3d_{5/2}$ orbital peaks.[29,37] A typical characteristic peak separation of ~8.5 eV is also observed.[37,38] In Figure 1e, the peak at 55.8 eV originates from the Se in SnSe,[39] whereas the peak observed at 59.2 eV is associated with Se^{4+}, which could be due to the surface oxidation during sample handling.[40] Figure 1f shows the high-resolution C 1s spectrum of SnSe@CNFs. The peaks at 284.6, 285.3, and 286.5 eV correspond to the C−C, C−N, and C═N bonds, respectively.[41] The existence of N originates from the self-doping from nitrogen-containing PAN precursor.[42,43] N-doped carbon is well-known to promote electronic conductivity because of the numerous N-doping-induced π-conjunctions among carbon.[44] Additionally, N-doping could introduce some surface defects that could enhance the exposure of more active sites.[45] The FeSe@CNFs XPS full survey is shown in Figure S3a, demonstrating the coexistence of Fe, C, and Se elements. Figure S3b shows the Fe 2p spectrum where the two strongest peaks at 710.5 and 724.7 eV correspond to the Fe $2p_{1/2}$ and Fe $2p_{3/2}$ spin−orbits of Fe^{2+}, respectively. The peak appearing at 713.5 eV is the satellite peak. The peak at 712.0 eV is ascribed to Fe^{3+}.[46] The Se 3d peak in Figure S3c shows the peaks at 58.0 and 55.0 eV, corresponding to Se $3d_{5/2}$ and Se $3d_{3/2}$ spin−orbits, respectively.[46] The peak at 58.9 eV corresponds to the Se−O bond.[47] The full survey of the NiSe@CNFs sample is presented in Figure S3d with the presence of Ni 2p, C 1s, Se 3d, and O 1s peak. The Ni 2p spectrum (Figure S3e) shows Ni^{2+}-originating peaks including the major peaks at 855.4 and 873.2 eV, and other shake-up satellite peaks.[48,49] In Figure S3f, the Se 3d peaks of NiSe@CNFs at 53.9 and 54.9 eV represent Se $3d_{3/2}$ and Se $3d_{5/2}$, respectively.[50−52] Moreover, there is a small peak at approximately 58.9 eV that is due to a trace of surface oxidation of the sample.[49] The full survey spectrum of Cu_2Se@CNFs is demonstrated in Figure S3g. The Cu 2p spectrum in Figure S3h shows the binding energies of Cu $2p_{3/2}$ and Cu $2p_{1/2}$ from Cu_2Se around 932.6 and 952.4 eV, respectively.[53] The presence of small shoulder peaks at 933.7 and 953.2 eV from Cu^{2+} is related to partial oxidation on the surface.[54,55] The Se 3d of Cu_2Se@CNFs in Figure S3i has the peaks among 54.8 and 56.6 eV from Se^{2-}.[56] Partial oxidation of the surface particles is indicated by the Se−O bond peak at 58.5 eV.[57]

The morphology and structure of MSe@CNFs samples are examined by SEM and TEM. Figure 2a–e displays the SEM

https://doi.org/10.1021/acsaem.1c03277
ACS Appl. Energy Mater. 2022, 5, 842−851

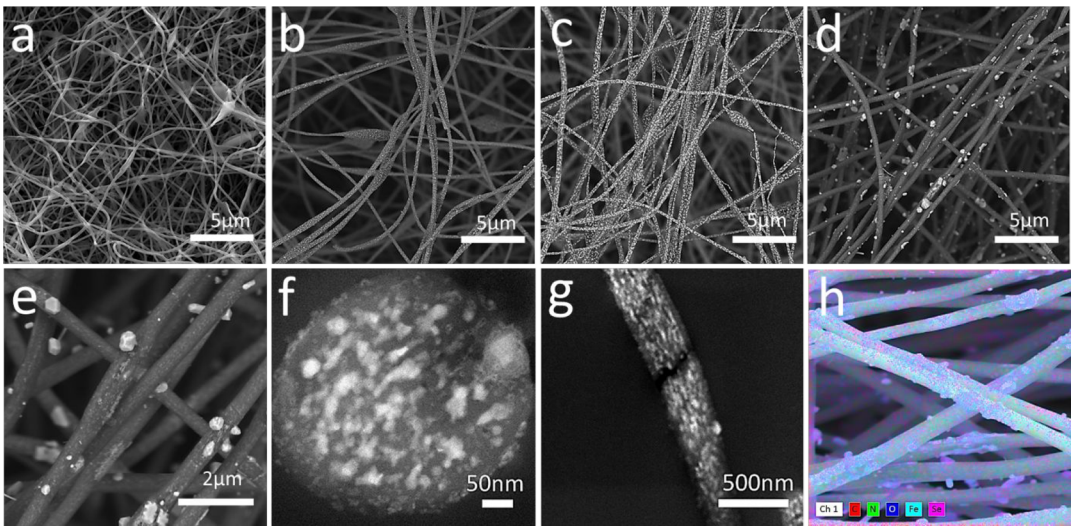

Figure 2. SEM images of (a) SnSe@CNFs; (b) Cu_2Se@CNFs; (c) NiSe@CNFs; (d) FeSe@CNFs; (e) higher-magnification SEM image of FeSe@CNFs; (f)cross-section TEM image of FeSe@CNFs; (g) longitudinal TEM image of FeSe@CNFs; and (h) overlapping EDX mapping image of FeSe@CNFs.

images of SnSe@CNFs, Cu_2Se@CNFs, NiSe@CNFs, and FeSe@CNFs. As expected, all samples have the morphology of nanofibers. No obvious metal selenide agglomerates or loose particles are observed in the samples. The carbon nanofibers intertwine with each other and form a three-dimensional network that can serve as a fast highway network for electron transfer. There are also plenty of empty spaces at the micrometer scale among the 3D network, which benefits the electrolyte penetration and fast ion transfer. In detail, the SnSe@CNFs sample presents a relatively smooth surface along the carbon nanofibers with no obvious particles observed. It could be the tin precursor annealing synthesis tends to generate ultrafine tin-based particles that are usually too small to observe at this magnification.[29,58] In contrast, FeSe@CNFs sample has some relatively large particles dispersed sparsely on the surface, whereas the NiSe@CNFs and Cu_2Se@CNFs samples have plenty of small particles densely packed along the carbon nanofiber. To observe the inner structures of the fiber, microtomed samples are examined with TEM further. Microtomed images of the FeSe@CNFs sample shown in Figure 2f,g are used as an example for demonstration. Both the longitudinal and cross-sectional images show most of the nanoparticles are densely packed inside the fibers. Only a few particles protruded out of the carbon nanofibers surface, in agreement with the SEM observation. Microstructures having nanoparticles firmly embedded in the carbon nanofiber matrixes can avoid agglomeration and greatly alleviate the stress from volume expansion during cycling. Figure 2h presents the EDX mapping of the FeSe@CNFs sample. Fe (teal) and Se (purple) elements can be observed and mostly overlap with each other, further indicating the formation of metal selenide. In addition, N (green) element doping can be clearly observed, which could benefit the electrical conductivity of the sample. Though carbon (red) forms the backbone of the sample, it is not clearly presented. It is due to the surface coverage of the metal selenide. The trace of O (blue) could be due to either adsorption of oxygen on the sample surfaces or partial oxidation of the sample surface during sample handling. These EDX results are in good agreement with the XPS results.

Cyclic voltammetry (CV) measurements were conducted to study the Li^+ storage behavior in a MSe@CNFs electrode. The first three CV curves of the SnSe@CNFs electrode tested at a scan rate of 0.2 mV s^{-1} are shown in Figure 3a. During the first sweep, the cathodic peak at 1 V can be ascribed to the conversion of SnSe to metallic Sn and Li_2Se ($SnSe + 2Li^+ + 2e^- \leftrightarrow Sn + Li_2Se$). The peak located around 0.4 V is attributed to the alloying reaction between Sn and Li^+ to form the Li_xSn alloy ($Sn + xLi^+ + xe^- \leftrightarrow Li_xSn$).[58−60] The oxidation peaks around 0.7 V are attributed to the multistep dealloying processes.[60] The oxidation peaks at 1.8 V could be attributed to the formation of SnSe.[61] After the first cycle, the following sweeps overlap well with each other, suggesting the good reversibility of the SnSe@CNFs anode material. The CV curves of other MSe@CNFs samples are shown in Figure S4a−c. The detailed discussion is available in the Supporting Information. Figure 3b presents the galvanostatic charge/discharge profile of the SnSe@CNFs electrode at 0.3 mA g^{-1}. There is an obvious voltage plateau at the first discharge curve, corresponding to the conversion of SnSe and the formation of solid electrolyte interphase (SEI) layers. An initial Coulombic efficiency (CE) of 72.6% is obtained. The mediocre initial Coulombic efficiency is due to the formation of SEI layers that lead to irreversible consumption of lithium ions. There is no significant decrease of capacity from the second to third cycle, suggesting good reversibility after the initial irreversible capacity loss. It is in good agreement with the CV result. The CEs of the second cycle and third cycle rise to 96.6% and 98.5%. Afterward, it approaches 100% and remains near 100% (Figure 3c), confirming good reversibility during the cycling process.

The long-term cycle performance of the MSe@CNFs as a lithium anode electrode was evaluated at the current density of 0.3 A g^{-1} for up to 80 cycles, shown in Figure 3c. The SnSe@CNFs, FeSe@CNFs, Cu_2Se@CNFs, and NiSe@CNFs electrodes exhibit an initial irreversible capacity of 828.2, 739.1, 631.6, and 641.8 mA h g^{-1}, respectively. After 80 cycles, the SnSe@CNFs deliver a specific capacity of 578 mA h g^{-1} with a 96% retention of the second discharge cycle. The discharge capacities after 80 cycles for FeSe@CNFs, Cu_2Se@CNFs,

https://doi.org/10.1021/acsaem.1c03277
ACS Appl. Energy Mater. 2022, 5, 842−851

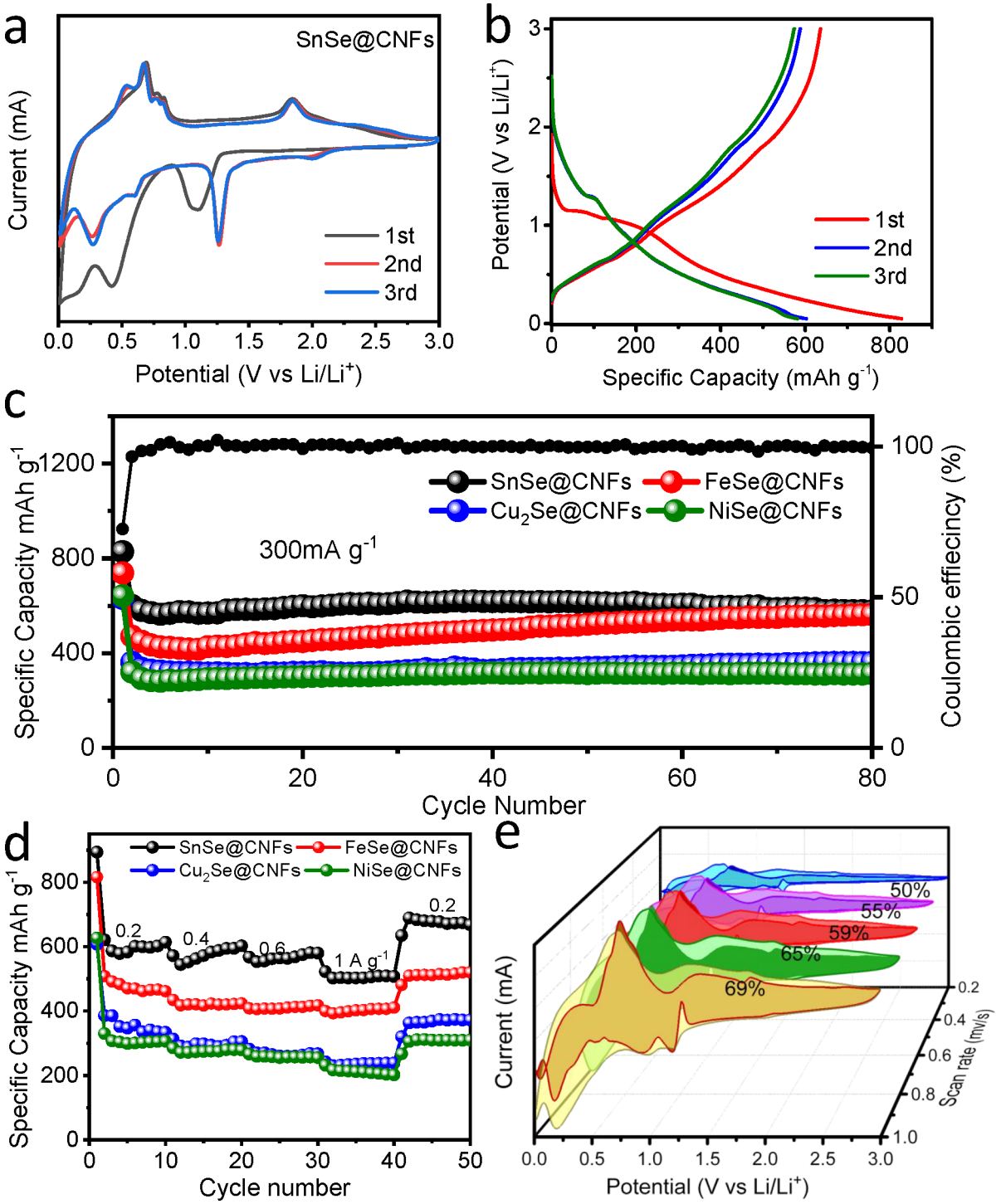

Figure 3. (a) CV profiles of the SnSe@CNFs electrode; (b) galvanostatic charge−discharge profiles of the SnSe@CNFs electrode at 300 mA g^{-1}; (c) cycle performance of the four samples at a current density of 300 mA g^{-1}; (b) rate performance of the four samples; (e) CV curves and contribution ratios of the capacitive charge of SnSe@CNFs electrode versus scan rate.

and NiSe@CNFs are 563, 362, and 314 mA h g^{-1} with a retention of 120%, 100%, and 98% of the second cycle, respectively. The slight capacity increment of the samples can be ascribed to the gradual activation of the electrode materials, which is frequently observed in transition-metal-based anode materials.[62−64] The above results demonstrate the good stability of the rationally designed MSe@CNFs electrode that possesses a robust structure to effectively buffer the stress of the volume change during the repeated lithiation and delithiation process.

Beside the cycle stability, good rate performance is also favorable for practical applications. Figure 3d presents the rate performance of the MSe@CNFs electrode, where the SnSe@CNFs electrode delivers a 10th cycle capacity of 614.0, 602.8, 580.2, and 507.4 mA h g^{-1} at 0.2, 0.4, 0.6, and 1 A g^{-1}, respectively; the FeSe@CNFs electrode provides a 10th cycle capacity of 461.5, 423.8, 418.0, and 411.1 mA h g^{-1} at 0.2, 0.4,

https://doi.org/10.1021/acsaem.1c03277
ACS Appl. Energy Mater. 2022, 5, 842−851

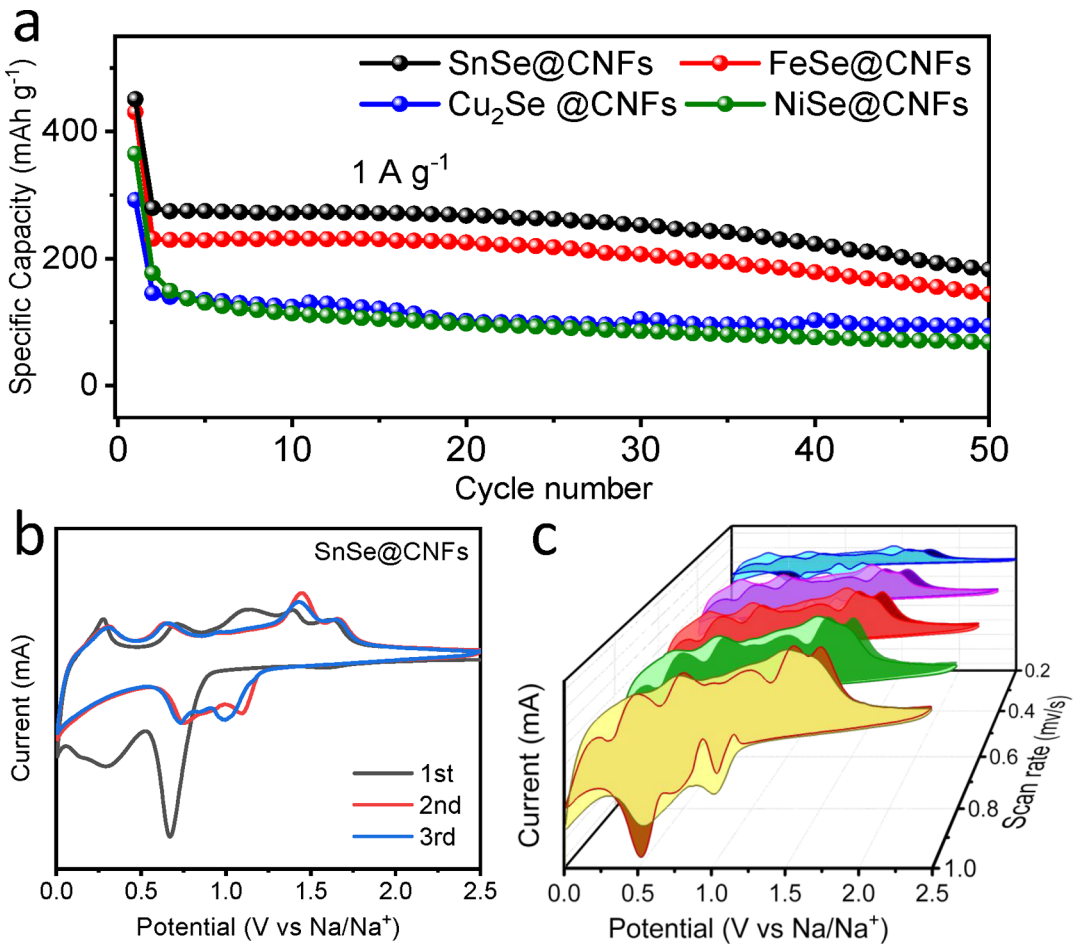

Figure 4. (a) SIB cycle performance of the four samples at a current density of 1 A g^{-1}; (b) CV profiles of the SnSe@CNFs electrode; (c) CV curves and contribution ratios of the capacitive of SnSe@CNFs electrode charge versus scan rate.

0.6, and 1 A g^{-1}, respectively. When the current density is decreased from 1 to 0.2 A g^{-1}, the capacities of SnSe@CNFs and FeSe@CNFs electrodes can rapidly go back to 634.8 and 481.2 mA h g^{-1}, indicating robust rate capability. Meanwhile, other MSe@CNFs electrodes show slightly lower capacities but a good ability to rapidly recover capacity from high current density cycling. The good rate performance could be attributed to the rationally designed structure that can promote fast Li^+ ion and electron transport. The well-designed 3D network allows the electrolyte to easily access the active materials through large voids as well as fast electron transfer enabled by the interconnected N-doped carbon fibers.

To further understand the lithium storage mechanism of the MSe@CNFs electrodes, stepwise CV measurements (0.2−1 V s^{-1}) were carried out. The relationship of the measured current as a function of potential, pseudocapacitive current, and diffusion-controlled current can be described with eq 1 according to Brezesinski et al.:[65]

$$i(V) = k_1\nu + k_2\nu^{1/2} \quad (1)$$

where $i(V)$ is the total current at the measured potential V, k_1 and k_2 are constants that can be determined by stepwise CV measurements, and ν is the scan rate. Thus, the contributions of each process can be quantitatively evaluated. The data was fit by online K-1 tool software to determine the k_1 and k_2 value.[66] The fitting results of the SnSe@CNFs electrode are shown in Figure 3e, where the inner region represents the pseudocapacitive contribution at different scan rates. The contribution ratio of pseudocapacitance is 50%, 55%, 59%, 65%, and 69% at 0.2, 0.4, 0.6, 0.8, and 1 mV s^{-1}, respectively. The results indicate that pseudocapacitive contributions are dominant and increase with the increase of the scan rate. This phenomenon could be due to the unique structure having numerous macrospores, allowing fast ion transfers to active sites as well as an integrated fast transfer network for electrons.[67] Conversely, the diffusion contribution decreases while the sweep rate increases, likely attributed to the increased ohmic resistance.[68]

The as-prepared materials are also explored in an SIB system. Figure 4a shows the cycle performance of the MSe@CNFs materials at a high current density of 1 A g^{-1}. The SnSe@CNFs, FeSe@CNFs, Cu_2Se@CNFs, and NiSe@CNFs electrodes exhibit an initial irreversible capacity of 451.1, 430.6, 364.9, and 292.2 mA h g^{-1}, respectively. The SnSe@CNFs delivers a capacity of 186.7 mA h g^{-1}, with a retention of 65% of the second cycle after 50 cycles. Meanwhile, the FeSe@CNFs electrode shows a 62% retention and 144.1 mA h g^{-1} at the 50th cycle. Other MSe@CNFs electrodes show lower but very stable capacities at a high current density up to 50 cycles. Such cycle performance at a high current density with low capacity fading over 50 cycles indicates these MSe@CNFs are highly promising to the SIBs system.

The Na^+ storage behavior was also investigated by CV measurements. The first three CV curves of the SnSe@CNFs

https://doi.org/10.1021/acsaem.1c03277
ACS Appl. Energy Mater. 2022, 5, 842−851

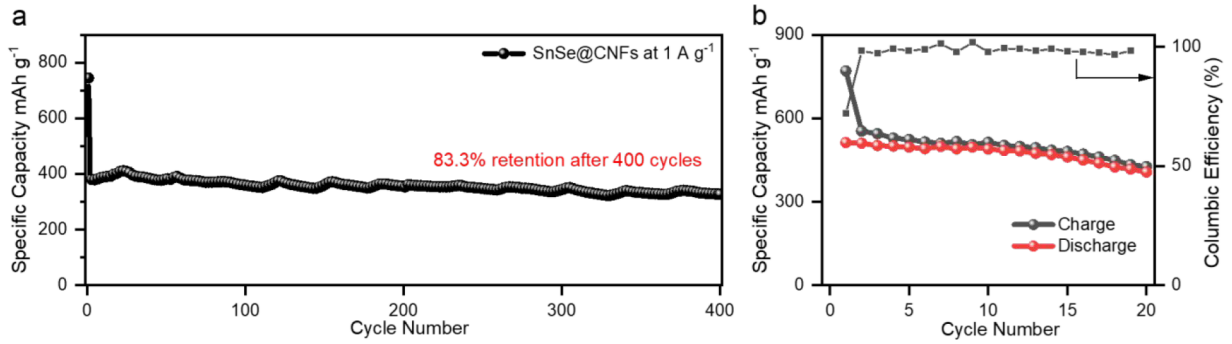

Figure 5. Cycling performance of (a) SnSe@CNFs in a half cell at 1 A g^{-1} for 400 cycles; (b) SnSe@CNFs//$LiFePO_4$ in a full cell at 0.1 A g^{-1}.

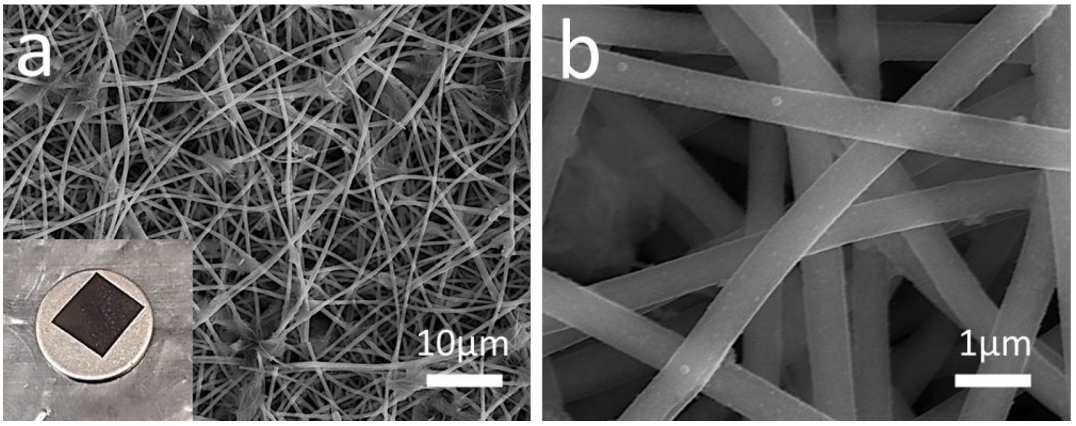

Figure 6. SEM images of FeSe@CNFs electrode (a) after 50 cycles; the inset is the digital picture of the cycled sample. (b) High-magnification image of the sample.

electrode are shown in Figure 4b. The large cathodic peak at 0.7 V in the first sweep can be ascribed to the conversion reaction of SnSe to Sn and Na_2Se ($SnSe + 2Na^+ + 2e^- \leftrightarrow Sn + Na_2Se$) and the formation of the SEI layer.[37] The broad peak below 0.5 V are usually ascribed to the progressive process of Na−Sn alloying reaction ($Sn + xNa^+ + xe^- \leftrightarrow Na_xSn$).[69] The oxidation peaks around 0.3−0.7 V during all anodic scan processes can be assigned to the multistep dealloying reaction from Na_xSn to Na−Sn intermediates and the final metallic Sn.[58] The oxidation peaks located at above 1.1 V are attributed to the extraction of Na^+ and reaction of Sn to SnSe.[58,70] In the subsequent scans, the two cathodic peaks shift to around 0.7 and 1 V, which could be described as the conversion and alloying reactions.[58,70] After the initial cycle, the following cycles overlap well with each other, indicating good reversibility of the electrode. The CV curves of other MSe@CNFs samples are shown and discussed in the Supporting Information (Figure S4d−f).

The sodium storage mechanism was also investigated by the stepwise CV measurements at different scan rates. Capacitance-controlled contribution at different scan rates is quantitatively calculated by the same method mentioned above. Figure 4c displays the contribution of the SnSe@CNFs electrode pseudocapacitance contribution, which are 72%, 76%, 80%, 83%, and 86% at 0.2, 0.4, 0.6, 0.8, and 1 mV s^{-1}, respectively. The result shows the pseudocapacitance is also the dominant form of sodium storage for the SnSe@CNFs anode electrode, similar to that found in a previous report.[71] At the different scan rates, a lower diffusion capacitance ratio is observed, in comparison with that in the LIBs system. The larger radius of the Na^+ ion (1.02 vs 0.76 Å of Li^+ ion) may lead to relatively sluggish reaction kinetics of sodiation/desodiation through the metal selenide electrode in SIBs, in comparison with the rapid lithiation/delithiation process in LIBs.[72]

Among all the tests, SnSe@CNFs exhibited the best performance among the four electrodes. It was therefore selected for further exploration of the long-term cyclic stability and full-cell performance in LIBs. As shown in Figure 5a, the SnSe@CNFs exhibits an initial capacity of 744.1 mA h g^{-1} at a high current density of 1 A g^{-1}. After 400 cycles, the electrode still maintains a capacity of 326.8 mA h g^{-1} with 83.3% retention compared to the second cycle. The full cell was assembled with commercial $LiFePO_4$ electrode (MTI Corporation, USA) as the cathode and SnSe@CNFs as the anode with an N/P ratio of ∼1.1. Testing voltage of the full cells ranged from 0.5 to 4 V with a 0.1 A g^{-1} current density. Calculations are based on the anode mass; the cell exhibits a high initial charge capacity of 770.3 mA h g^{-1} with an initial CE of 72.0%. After 20 cycles, the reversible charge capacity is still maintained at 426.4 mA h g^{-1} with nearly 100% CE, showing relatively good reversibility.

Overall, the as-prepared MSe@CNFs demonstrates good cyclability and rate performance in both LIBs and SIBs. The good electrochemical performance is attributed to their unique structure. For further evaluation of their structural stability, postmortem examination was performed. The lithium cells after cycling were disassembled in glovebox and imaged by SEM. The digital picture of the cycled FeSe@CNFs electrode is shown in the inset of Figure 6a. As can be seen, the cycled electrode still maintains its original appearance without visible breakage or cracks. The SEM images in Figure 6a,b shows the

https://doi.org/10.1021/acsaem.1c03277
ACS Appl. Energy Mater. 2022, 5, 842−851

electrode still maintains the intact fibrous morphology of a continuously interconnected 3D network after 50 cycles at the current density of 300 mA/g. The SEM images of SnSe@CNFs electrode after 50 cycles and 400 cycles at a high current density of 1 A/g are shown in Figure S5; the fibrous morphology is also maintained. The fibers of the electrode seem bigger in diameter after 400 cycles, which could be ascribed to the continuous formation of the SEI layer. Overall, the well-maintained 3D fiber structure and unbroken individual fibers indicate the remarkable structural stability of the MSe@CNFs electrode.

4. CONCLUSIONS

In summary, a series of MSe@CNFs binderless, free-standing electrodes have been successfully prepared by a generalized approach based on electrospinning and a subsequent annealing process. The free-standing MSe@CNFs electrodes were thoroughly investigated, showing promising electrochemical cyclability and rate capability in both LIBs and SIBs systems. The enhanced performance is achieved by the well-designed composite structure that is capable of promoting the ionic and electronic transport and alleviating the stress resulting from the volume change during repeated charging and discharging processes. The results reported here indicate the generalized method is highly promising to prepare binderless, free-standing metal selenides and carbon nanofibers composites for lightweight and high-performance batteries.

■ ASSOCIATED CONTENT

Supporting Information

The Supporting Information is available free of charge at https://pubs.acs.org/doi/10.1021/acsaem.1c03277.

Additional experimental details and results, including photographs of samples, XPS, TGA, CV, and SEM data (PDF)

■ AUTHOR INFORMATION

Corresponding Authors

Xiao-Dong Zhou − *Department of Chemical Engineering, Institute for Materials Research and Innovations, University of Louisiana at Lafayette, Lafayette, Louisiana 70504, United States*; Email: xiao-dong.zhou@louisiana.edu

Ling Fei − *Department of Chemical Engineering, Institute for Materials Research and Innovations, University of Louisiana at Lafayette, Lafayette, Louisiana 70504, United States*; orcid.org/0000-0002-0954-5168; Email: ling.fei@louisiana.edu

Authors

Zizhou He − *Department of Chemical Engineering, Institute for Materials Research and Innovations, University of Louisiana at Lafayette, Lafayette, Louisiana 70504, United States*

Hui Guo − *Department of Chemical Engineering, Institute for Materials Research and Innovations, University of Louisiana at Lafayette, Lafayette, Louisiana 70504, United States*

Jed D. LaCoste − *Department of Chemical Engineering, Institute for Materials Research and Innovations, University of Louisiana at Lafayette, Lafayette, Louisiana 70504, United States*

Don Werder − *Cornell Center for Materials Research, Cornell University, Ithaca, New York 14853, United States; Department of Materials Science and Engineering and Platform for the Accelerated Realization, Analysis, and Discovery of Interface Materials (PARADIM), Cornell University, Ithaca, New York 14853, United States*

Derek J. Durocher − *Department of Chemical Engineering, Institute for Materials Research and Innovations, University of Louisiana at Lafayette, Lafayette, Louisiana 70504, United States*

Ryan A. Cook − *Department of Chemical Engineering, Institute for Materials Research and Innovations, University of Louisiana at Lafayette, Lafayette, Louisiana 70504, United States*

Phat Truong − *Department of Chemical and Materials Engineering, New Mexico State University, Las Cruces, New Mexico 88003, United States*

Hongmei Luo − *Department of Chemical and Materials Engineering, New Mexico State University, Las Cruces, New Mexico 88003, United States*; orcid.org/0000-0002-9546-761X

Complete contact information is available at: https://pubs.acs.org/10.1021/acsaem.1c03277

Notes

The authors declare no competing financial interest.

■ ACKNOWLEDGMENTS

L.F. acknowledges financial support from the National Science Foundation (Award Number 1832963) and Chevron Corporation for providing the Chevron Endowed Professorship in Chemical Engineering at UL Lafayette. X.D.Z. and L.F. are thankful for the support from NSF under NSF-2119688 and NASA# 80NSSC21M0333. L.F. also acknowledges facility support from the NSF MRI Program (NSF-1920166). This work also made use of the Cornell Center for Materials Research Facilities supported by the National Science Foundation under Award Number DMR-1719875 and was supported by NSF Platform for the Accelerated Realization, Analysis and Discovery of Interface Materials (PARADIM) under Cooperative Agreement No. 2039380. D.J.D. and R.A.C. acknowledge the support from the UL Lafayette College of Engineering Research Apprentice program.

■ REFERENCES

(1) Carrilero, I.; González, M.; Anseán, D.; Viera, J. C.; Chacón, J.; Pereirinha, P. G. Redesigning European public transport: impact of new battery technologies in the design of electric bus fleets. *Transp. Res. Procedia* **2018**, *33*, 195−202.

(2) Wang, K.; Luo, S.; Wu, Y.; He, X.; Zhao, F.; Wang, J.; Jiang, K.; Fan, S. Super-aligned carbon nanotube films as current collectors for lightweight and flexible lithium ion batteries. *Adv. Funct. Mater.* **2013**, *23* (7), 846−853.

(3) Armand, M.; Tarascon, J. M. Building better batteries. *Nature* **2008**, *451* (7179), 652−657.

(4) Janek, J.; Zeier, W. G. A solid future for battery development. *Nat. Energy* **2016**, *1* (9), 16141.

(5) Sun, W.; Tang, X.; Wang, Y. Multi-metal−Organic Frameworks and Their Derived Materials for Li/Na-Ion Batteries. *Electrochem. Energy Rev.* **2020**, *3* (1), 127−154.

(6) Lei, Y. J.; Yan, Z. C.; Lai, W. H.; Chou, S. L.; Wang, Y. X.; Liu, H. K.; Dou, S. X. Tailoring MXene-Based Materials for Sodium-Ion Storage: Synthesis, Mechanisms, and Applications. *Electrochem. Energy Rev.* **2020**, *3* (4), 766−792.

(7) Xie, F.; Xu, Z.; Guo, Z.; Titirici, M. M. Hard carbons for sodium-ion batteries and beyond. *Prog. Energy* **2020**, *2* (4), 042002.

(8) Wang, L.; Wei, Z.; Mao, M.; Wang, H.; Li, Y.; Ma, J. Metal oxide/graphene composite anode materials for sodium-ion batteries. *Energy Storage Mater.* **2019**, *16*, 434−454.
(9) Lu, J.; Chen, Z.; Pan, F.; Cui, Y.; Amine, K. High-performance anode materials for rechargeable lithium-ion batteries. *Electrochem. Energy. Rev.* **2018**, *1* (1), 35−53.
(10) Ali, Z.; Asif, M.; Huang, X.; Tang, T.; Hou, Y. Hierarchically porous fe_2cose_4 binary-metal selenide for extraordinary rate performance and durable anode of sodium-ion batteries. *Adv. Mater.* **2018**, *30*, 1802745.
(11) Liu, J.; Gu, M.; Ouyang, L.; Wang, H.; Yang, L.; Zhu, M. Sandwich-like SnS/Polypyrrole Ultrathin Nanosheets as High-Performance Anode Materials for Li-Ion Batteries. *ACS Appl. Mater. Interfaces* **2016**, *8* (13), 8502−10.
(12) Xu, X.; Liu, J.; Liu, Z.; Shen, J.; Hu, R.; Liu, J.; Ouyang, L.; Zhang, L.; Zhu, M. Robust Pitaya-Structured Pyrite as High Energy Density Cathode for High-Rate Lithium Batteries. *ACS Nano* **2017**, *11* (9), 9033−9040.
(13) Xu, X.; Liu, Z.; Ji, S.; Wang, Z.; Ni, Z.; Lv, Y.; Liu, J.; Liu, J. Rational synthesis of ternary FeS@TiO2@C nanotubes as anode for superior Na-ion batteries. *Chem. Eng. J.* **2019**, *359*, 765−774.
(14) Liu, Y.; Zhang, N.; Yu, C.; Jiao, L.; Chen, J. $MnFe_2O_4$@C nanofibers as high-performance anode for sodium-ion batteries. *Nano Lett.* **2016**, *16* (5), 3321−8.
(15) Xu, X.; Liu, J.; Liu, J.; Ouyang, L.; Hu, R.; Wang, H.; Yang, L.; Zhu, M. A general metal-organic framework (MOF)-derived selenidation strategy for in situ carbon-encapsulated metal selenides as high-rate anodes for Na-ion batteries. *Adv. Funct. Mater.* **2018**, *28*, 1707573.
(16) Shiga, Y.; Umezawa, N.; Srinivasan, N.; Koyasu, S.; Sakai, E.; Miyauchi, M. A metal sulfide photocatalyst composed of ubiquitous elements for solar hydrogen production. *Chem. Commun.* **2016**, *52* (47), 7470−3.
(17) Huang, L.; Chen, Z.; Li, J. Effects of strain on the band gap and effective mass in two-dimensional monolayer GaX (X = S, Se, Te). *RSC Adv.* **2015**, *5* (8), 5788−5794.
(18) Xia, X.; Wang, L.; Sui, N.; Colvin, V. L.; Yu, W. W. Recent Progress in Transition Metal Selenide Electrocatalysts for Water Splitting. *Nanoscale* **2020**, *12*, 12249−12262.
(19) Zhou, H.; Li, X.; Li, Y.; Zheng, M.; Pang, H. Applications of M_xSe_y (M = Fe, Co, Ni) and Their Composites in Electrochemical Energy Storage and Conversion. *Nanomicro. Lett.* **2019**, *11* (1), 40.
(20) Xiang Huang, Z.; Liu, B.; Kong, D.; Wang, Y.; Ying Yang, H. $SnSe_2$ quantum dot/rGO composite as high performing lithium anode. *Energy Storage Mater.* **2018**, *10*, 92−101.
(21) Zhong, D.; Chen, J.; Zhang, J.; Luo, Y.; Li, Z.; Cheng, L.; Chen, Y.; Wang, G.; Wang, R. The yolk-shell FeSe@C nanobox with novel synthesis and its high performance for the anode of lithium-ion batteries. *Mater. Res. Express* **2019**, *6* (8), 085058.
(22) Gao, T.-P.; Wong, K. W.; Ng, K. M. Impacts of morphology and N-doped carbon encapsulation on electrochemical properties of NiSe for lithium storage. *Energy Storage Mater.* **2020**, *25*, 210−216.
(23) Xiong, Z.; Sun, D.; Jia, X.; Zhou, J. Core/shell FeSe/carbon nanosheet-assembled microflowers with ultrahigh coulombic-efficiency and rate performance as nonpresodiate anode for sodium-ion battery. *Carbon* **2020**, *166*, 339−349.
(24) Dong, S.; Su, Q.; Jiao, W.; Ding, S.; Zhang, M.; Du, G.; Xu, B. $FeSe_2$ microspheres coated with carbon layers as anode materials for sodium-ion batteries. *J. Alloys Compd.* **2020**, *842*, 155888.
(25) Su, C.; Ru, Q.; Cheng, S.; Gao, Y.; Chen, F.; Zhao, L.; Ling, F. C.-C. 3D pollen-scaffolded NiSe composite encapsulated by MOF-derived carbon shell as a high-low temperature anode for Na-ion storage. *Composites, Part B* **2019**, *179*, 107538.
(26) Luo, M.; Yu, H.; Hu, F.; Liu, T.; Cheng, X.; Zheng, R.; Bai, Y.; Shui, M.; Shu, J. Metal selenides for high performance sodium ion batteries. *Chem. Eng. J.* **2020**, *380*, 122557.
(27) Hu, Z.; Liu, Q.; Chou, S. L.; Dou, S. X. Advances and Challenges in Metal Sulfides/Selenides for Next-Generation Rechargeable Sodium-Ion Batteries. *Adv. Mater.* **2017**, *29* (48), 1700606.
(28) Jin, T.; Han, Q.; Jiao, L. Binder-Free Electrodes for Advanced Sodium-Ion Batteries. *Adv. Mater.* **2020**, *32* (3), 1806304.
(29) Fei, L.; Williams, B. P.; Yoo, S. H.; Carlin, J. M.; Joo, Y. L. A general approach to fabricate free-standing metal sulfide@carbon nanofiber networks as lithium ion battery anodes. *Chem. Commun.* **2016**, *52* (7), 1501−4.
(30) Ma, T. Y.; Dai, S.; Qiao, S. Z. Self-supported electrocatalysts for advanced energy conversion processes. *Mater. Today* **2016**, *19* (5), 265−273.
(31) Zhu, Z.; Wang, S.; Du, J.; Jin, Q.; Zhang, T.; Cheng, F.; Chen, J. Ultrasmall Sn nanoparticles embedded in nitrogen-doped porous carbon as high-performance anode for lithium-ion batteries. *Nano Lett.* **2014**, *14* (1), 153−7.
(32) Yin, B.; Cao, X.; Pan, A.; Luo, Z.; Dinesh, S.; Lin, J.; Tang, Y.; Liang, S.; Cao, G. Encapsulation of CoS_x nanocrystals into N/S Co-doped honeycomb-like 3D porous carbon for high-performance lithium storage. *Adv. Sci.* **2018**, *5* (9), 1800829.
(33) He, Z.; Guo, H.; LaCoste, J. D.; Cook, R. A.; Hussey, B.; Zhang, X.; Gang, D. D.; Hao, J.; Chen, L.; Cooke, P.; Yan, H.; Fei, L. Directly embedded Ni_3S_2/Co_9S_8@S-doped carbon nanofiber networks as a free-standing anode for lithium-ion batteries. *Sustain. Energy Fuels* **2021**, *5* (1), 166−174.
(34) Wang, Z.; Kang, K.; Wu, J.; Hu, Q.; Harper, D. P.; Du, G.; Wang, S.; Xu, K. Comparative effects of electrospinning ways for fabricating green, sustainable, flexible, porous, nanofibrous cellulose/chitosan carbon mats as anode materials for lithium-ion batteries. *J. Mater. Res. Technol.* **2021**, *11*, 50−61.
(35) Lian, X.; Xu, N.; Ma, Y.; Hu, F.; Wei, H.; Chen, H.-Y.; Wu, Y.; Li, L.; Li, D.; Peng, S. In-situ formation of $Co_{1-x}S$ hollow polyhedrons anchored on multichannel carbon nanofibers as self-supporting anode for lithium/sodium-ion batteries. *Chem. Eng. J.* **2021**, *421*, 127755.
(36) Ge, X.; Liu, S.; Qiao, M.; Du, Y.; Li, Y.; Bao, J.; Zhou, X. Enabling Superior electrochemical properties for highly efficient potassium storage by impregnating ultrafine sb nanocrystals within nanochannel-containing carbon nanofibers. *Angew. Chem., Int. Ed.* **2019**, *58* (41), 14578−14583.
(37) Park, G. D.; Lee, J. H.; Kang, Y. C. Superior Na-ion storage properties of high aspect ratio SnSe nanoplates prepared by a spray pyrolysis process. *Nanoscale* **2016**, *8* (23), 11889−96.
(38) Ling, L.; Zhang, Q.; Zhu, L.; Wang, C.-F.; Chen, S. Interfacial synthesis of SnSe quantum dots for sensitized solar cells. *RSC Adv.* **2015**, *5* (3), 2155−2158.
(39) Park, G. D.; Lee, J.-K.; Chan Kang, Y. Design and synthesis of Janus-structured mutually doped $SnO_2-Co_3O_4$ hollow nanostructures as superior anode materials for lithium-ion batteries. *J. Mater. Chem. A* **2017**, *5* (48), 25319−25327.
(40) Li, X.; Lv, W.; Wu, G.; Fu, G.; Zhang, W.; Li, Z. A novel CuSe-$Cu_{1.8}Se$ heterostructure with hexahedral structure cathode material for aluminum batteries. *Chem. Eng. J.* **2021**, *426*, 131899.
(41) Zhou, P.; Zhang, M.; Wang, L.; Huang, Q.; Su, Z.; Li, L.; Wang, X.; Li, Y.; Zeng, C.; Guo, Z. Synthesis and electrochemical performance of ZnSe electrospinning nanofibers as an anode material for lithium ion and sodium ion batteries. *Front. Chem.* **2019**, *7*, 569.
(42) Li, X.; Zhao, Y.; Bai, Y.; Zhao, X.; Wang, R.; Huang, Y.; Liang, Q.; Huang, Z. A non-woven network of porous nitrogen-doping carbon nanofibers as a binder-free electrode for supercapacitors. *Electrochim. Acta* **2017**, *230*, 445−453.
(43) Kim, J.-G.; Kim, H.-C.; Kim, N. D.; Khil, M.-S. N-doped hierarchical porous hollow carbon nanofibers based on PAN/PVP@SAN structure for high performance supercapacitor. *Composites, Part B* **2020**, *186*, 107825.
(44) Tian, Y. H.; Huang, J.; Sheng, X.; Sumpter, B. G.; Yoon, M.; Kertesz, M. Nitrogen Doping Enables Covalent-like pi-pi Bonding Between Graphenes. *Nano Lett.* **2015**, *15* (8), 5482−91.
(45) Shen, W.; Wang, C.; Xu, Q.; Liu, H.; Wang, Y. Nitrogen-doping-induced Defects of a Carbon Coating Layer Facilitate Na-Storage in Electrode Materials. *Adv. Energy Mater.* **2015**, *5* (1), 1400982.

https://doi.org/10.1021/acsaem.1c03277
ACS Appl. Energy Mater. 2022, 5, 842−851

(46) Chen, Y.; Shao, J.; Lin, X.; Gu, Y.; Holze, R.; Yun, Y.; Qu, Q.; Zheng, H. Hollow structured Carbon@FeSe nanocomposite as a promising anode material for Li-ion batteries. *ChemElectroChem* **2019**, *6* (5), 1393−1399.
(47) Lu, S.; Wu, H.; Xu, S.; Wang, Y.; Zhao, J.; Li, Y.; Abdelkader, A. M.; Li, J.; Wang, W.; Xi, K.; Guo, Y.; Ding, S.; Gao, G.; Kumar, R. V. Iron Selenide Microcapsules as Universal Conversion-typed Anodes for Alkali Metal-ion Batteries. *Small* **2021**, *17* (8), 2005745.
(48) Mao, X.; Gu, X.; Wen, S.; Zhang, L.; Dai, P.; Li, L.; Liu, D.; Li, D.; Li, Z.; Zhang, K.; Zhao, X. Carbon-coated NiSe nanoparticles anchored on reduced graphene oxide: a high-rate and long-life anode for potassium-ion batteries. *Sustain. Energy Fuels* **2021**, *5* (12), 3240−3246.
(49) Xu, Y.-Z.; Yuan, C.-Z.; Chen, X.-P. Co-Doped NiSe nanowires on nickel foam via a cation exchange approach as efficient electrocatalyst for enhanced oxygen evolution reaction. *RSC Adv.* **2016**, *6* (108), 106832−106836.
(50) Zou, Z.; Wang, X.; Huang, J.; Wu, Z.; Gao, F. An Fe-doped nickel selenide nanorod/nanosheet hierarchical array for efficient overall water splitting. *J. Mater. Chem. A* **2019**, *7* (5), 2233−2241.
(51) Mandale, A. B.; Badrinarayanan, S.; Date, S. K.; Sinha, A. P. B. Photoelectron-spectroscopic study of nickel, manganese and cobalt selenides. *J. Electron Spectrosc. Relat. Phenom.* **1984**, *33* (1), 61−72.
(52) Jiang, Q.-S.; Li, W.; Wu, J.; Cheng, W.; Zhu, J.; Yan, Z.; Wang, X.; Ju, Y. Electrodeposited cobalt and nickel selenides as high-performance electrocatalytic materials for dye-sensitized solar cells. *J. Mater. Sci.: Mater. Electron.* **2019**, *30* (10), 9429−9437.
(53) Hu, L.; Shang, C.; Akinoglu, E. M.; Wang, X.; Zhou, G. Cu_2Se Nanoparticles encapsulated by nitrogen-doped carbon nanofibers for efficient sodium storage. *Nanomaterials* **2020**, *10* (2), 302.
(54) Chen, C.; Liu, X.; Fang, Q.; Chen, X.; Liu, T.; Zhang, M. Self-assembly synthesis of CuO/ZnO hollow microspheres and their photocatalytic performance under natural sunlight. *Vacuum* **2020**, *174*, 109198.
(55) Ogwu, A. A.; Darma, T. H. A reactive magnetron sputtering route for attaining a controlled core-rim phase partitioning in Cu_2O/CuO thin films with resistive switching potential. *J. Appl. Phys.* **2013**, *113* (18), 183522.
(56) Ou, W.; Zou, Y.; Wang, K.; Gong, W.; Pei, R.; Chen, L.; Pan, Z.; Fu, D.; Huang, X.; Zhao, Y.; Lu, W.; Jiang, J. Active manipulation of NIR plasmonics: the case of $Cu_{2-x}Se$ through electrochemistry. *J. Phys. Chem. Lett.* **2018**, *9* (2), 274−280.
(57) Eikey, E. A.; Gan, X. Y.; Kaseman, D. C.; Murphey, C. G. E.; Crawford, S. E.; Johnston, K. A.; Yazdi, S.; Millstone, J. E. Efficient control of atom arrangement in ternary metal chalcogenide nanoparticles using precursor oxidation state. *Chem. Mater.* **2020**, *32* (3), 1322−1331.
(58) Xia, J.; Yuan, Y.; Yan, H.; Liu, J.; Zhang, Y.; Liu, L.; Zhang, S.; Li, W.; Yang, X.; Shu, H.; Wang, X.; Cao, G. Electrospun SnSe/C nanofibers as binder-free anode for lithium−ion and sodium-ion batteries. *J. Power Sources* **2020**, *449*, 227559.
(59) Lee, D. H.; Park, C. M. Tin selenides with layered crystal structures for Li-ion batteries: interesting phase change mechanisms and outstanding electrochemical behaviors. *ACS Appl. Mater. Interfaces* **2017**, *9* (18), 15439−15448.
(60) Lorie Lopez, J. L.; Grandinetti, P. J.; Co, A. C. Phase transformations and capacity fade mechanism in Li_xSn nanoparticle electrodes revealed by operando ^{7}Li NMR. *J. Mater. Chem. A* **2019**, *7* (17), 10781−10794.
(61) Zhang, L.; Lu, L.; Zhang, D.; Hu, W.; Wang, N.; Xu, B.; Li, Y.; Zeng, H. Dual-buffered SnSe@CNFs as negative electrode with outstanding lithium storage performance. *Electrochim. Acta* **2016**, *209*, 423−429.
(62) Yu, H.; Fan, H.; Yadian, B.; Tan, H.; Liu, W.; Hng, H. H.; Huang, Y.; Yan, Q. General approach for MOF-derived porous spinel AFe_2O_4 hollow structures and their superior lithium storage properties. *ACS Appl. Mater. Interfaces* **2015**, *7* (48), 26751−26757.
(63) Cao, W.; Wang, W.; Shi, H.; Wang, J.; Cao, M.; Liang, Y.; Zhu, M. Hierarchical three-dimensional flower-like Co_3O_4 architectures with a mesocrystal structure as high capacity anode materials for long-lived lithium-ion batteries. *Nano Res.* **2018**, *11* (3), 1437−1446.
(64) Yang, T.; Liu, Y.; Yang, D.; Deng, B.; Huang, Z.; Ling, C. D.; Liu, H.; Wang, G.; Guo, Z.; Zheng, R. Bimetallic metal-organic frameworks derived Ni-Co-Se@C hierarchical bundle-like nanostructures with high-rate pseudocapacitive lithium ion storage. *Energy Storage Mater.* **2019**, *17*, 374−384.
(65) Brezesinski, T.; Wang, J.; Tolbert, S. H.; Dunn, B. Ordered mesoporous alpha-MoO3 with iso-oriented nanocrystalline walls for thin-film pseudocapacitors. *Nat. Mater.* **2010**, *9* (2), 146−51.
(66) Liang, J.; Fan, Z.; Chen, S.; Zheng, S.; Wang, Z. A novel three-dimensional cross-linked net structure of submicron Si as high-performance anode for LIBs. *J. Alloys Compd.* **2021**, *860*, 158433.
(67) Fang, G.; Wu, Z.; Zhou, J.; Zhu, C.; Cao, X.; Lin, T.; Chen, Y.; Wang, C.; Pan, A.; Liang, S. Observation of pseudocapacitive effect and fast ion diffusion in bimetallic sulfides as an advanced sodium-ion battery anode. *Adv. Energy Mater.* **2018**, *8* (19), 1703155.
(68) Jagadale, A.; Zhou, X.; Blaisdell, D.; Yang, S. Carbon nanofibers (CNFs) supported cobalt- nickel sulfide ($CoNi_2S_4$) nanoparticles hybrid anode for high performance lithium ion capacitor. *Sci. Rep.* **2018**, *8* (1), 1602.
(69) Ren, X.; Wang, J.; Zhu, D.; Li, Q.; Tian, W.; Wang, L.; Zhang; Miao, L.; Chu, P. K.; Huo, K. Sn-C bonding riveted SnSe nanoplates vertically grown on nitrogen-doped carbon nanobelts for high-performance sodium-ion battery anodes. *Nano Energy* **2018**, *54*, 322−330.
(70) Yang, X.; Zhang, R.; Chen, N.; Meng, X.; Yang, P.; Wang, C.; Zhang, Y.; Wei, Y.; Chen, G.; Du, F. Assembly of SnSe nanoparticles confined in graphene for enhanced sodium-ion storage performance. *Chem. - Eur. J.* **2016**, *22* (4), 1445−51.
(71) Fleischmann, S.; Mitchell, J. B.; Wang, R.; Zhan, C.; Jiang, D.-e.; Presser, V.; Augustyn, V. Pseudocapacitance: from fundamental understanding to high power energy storage materials. *Chem. Rev.* **2020**, *120* (14), 6738−6782.
(72) Wen, J.; Xu, L.; Wang, J.; Xiong, Y.; Ma, J.; Jiang, C.; Cao, L.; Li, J.; Zeng, M. Lithium and potassium storage behavior comparison for porous nanoflaked Co_3O_4 anode in lithium-ion and potassium-ion batteries. *J. Power Sources* **2020**, *474*, 228491.

https://doi.org/10.1021/acsaem.1c03277
ACS Appl. Energy Mater. 2022, 5, 842−851